Ceramics International 49 (2023) 20968–20979

Contents lists available at ScienceDirect

Ceramics International

journal homepage: www.elsevier.com/locate/ceramint

Influence of ink rheology and post processing in the structural performance of silicon nitride-based ceramics fabricated by robocasting

M.S. Faria [a], M.F.R.P. Alves [a], R. Cintra [a], F.J. Oliveira [a], C.M. Fernandes [b], D. Figueiredo [b], S.M. Olhero [a,*]

[a] CICECO - Aveiro Institute of Materials, Department of Materials and Ceramic Engineering, University of Aveiro, 3810-193, Aveiro, Portugal
[b] Palbit, S.A., P.O. Box 4, 3854-908, Branca, Albergaria-a-Velha, Portugal

ARTICLE INFO

Handling Editor: P. Vincenzini

Keywords:
Si_3N_4 ceramics
Additive manufacturing
Robocasting
Inks
Rheology
Density
Flexural strength
Hardness
Microstructure

ABSTRACT

The fabrication of complex shaped Si_3N_4 parts by conventional methods is challenging due to its high hardness and mechanical strength. Additive manufacturing (AM) appeared as a competitive way to attain three-dimensional complexity at lower costs. However, most of AM technologies still present limitations in producing high dense ceramics, mainly due to several difficulties in developing proper feedstock. This work presents the fabrication of dense silicon nitride-based ceramics by using an extrusion based additive manufacturing technique (direct ink writing, also known as robocasting) and cold isostatic pressing (CIP) as a post processing step. Silicon-nitride aqueous based inks containing different amounts of solids loading (36, 38 and 39 vol%) and proper rheological characteristics for the printing process were studied. The use of CIP (200 MPa) is suggested to reduce or even eliminate defects and porosity and consequently, to improve mechanical performance of the final parts. Relative density, microhardness and flexural strength increased as solids loading in the inks increased and were further improved when CIP pressing was used. Parts produced by robocasting with an ink containing 39 vol% and cold isostatic pressed at 200 MPa exhibited an average relative density around 99%, 1475 HV2 microhardness value and 650 MPa flexural strength, values similar to those of silicon nitride ceramics fabricated by conventional processing.

1. Introduction

Silicon nitride (Si_3N_4) is a well-established ceramic material for several structural applications at room temperature and also high temperatures, thanks to its combination of properties, such as mechanical strength, hardness, wear resistance and thermal shock resistance [1]. Cutting tools, protection against high speed impacts and biomedical devices are examples of application fields for this material [2]. These ceramics are commonly produced industrially by powder processing followed by distinct sintering processes to attain high densification levels, a mandatory feature to achieve the expected high performance [3–5]. In fact, the covalent nature of the chemical bonds in Si_3N_4 makes the achievement of full densification a challenge. Dense materials can, however, be easily produced using pressure assisted techniques such as hot-pressing (HP) or hot isostatic pressing (HIP) [4]. Unfortunately, both techniques greatly increase the costs of the produced parts. The alternative, known as “pressureless sintering”, also uses a variety of sintering additives [6,7], albeit in larger amounts than the pressured assisted high temperature processing. Numerous mixes of different additives have been used, with a high emphasis on Al_2O_3 and Y_2O_3 [8]. During high temperature processing, these sintering additives react with the silicon oxide that spontaneously coats the Si_3N_4 powders, creating a liquid phase at temperatures lower than the decomposition temperature of Si_3N_4. This liquid can wet the Si_3N_4 particles, facilitating their decomposition, diffusion and reprecipitation.

To obtain complex geometries of Si_3N_4 ceramics by conventional processing, machining post-processes are commonly used, which are time-consuming, costly and unsustainable [4,5]. Additive manufacturing (AM) technologies could be an alternative and promising solution to fabricate Si_3N_4 based ceramic parts, due to their ability to form complex forms and fine details, in a bottom up approach, thus reducing significantly the disadvantages of the conventional processing [9,10]. The trend in using AM in ceramics has been growing, although several difficulties have been reported that explain their slow

* Corresponding author.
E-mail address: susana.olhero@ua.pt (S.M. Olhero).

https://doi.org/10.1016/j.ceramint.2023.03.231
Received 22 December 2022; Received in revised form 2 March 2023; Accepted 23 March 2023
Available online 24 March 2023

advancements when compared with AM of metals or polymers [11,12]. Concerning Si_3N_4 ceramics, reaching high densities and adequate mechanical performance are the main drawbacks for industrial implementation, mainly due to the complications in developing the proper feedstock for each AM technology [13]. Binder jetting (BJ), selective laser sintering (SLS), selective laser melting (SLM), Stereolithography (SLA), Digital Light Processing (DLP), Direct Ink Writing (DIW/robocasting) and direct photo shaping (an AM technique which combines robocasting with photocuring), have been the technologies mentioned to date in literature for the AM of Si_3N_4 ceramics [9,12,13]. Powder-based AM technologies, such as BJ and SLS, commonly uses granulated powders as feedstock to achieve a proper printing flow. The main concerns are related to the high porosity in the final parts [13,14]. Regarding technologies that use suspensions as feedstock, such as photopolymerization (SLA and/or DLP) and extrusion based categories (DIW/robocasting), maximization of the amount of ceramic powders in the pastes or suspensions, their homogeneity and stability over time, the rheological characteristics, the burnout of binders and large shrinkages of the final parts are still the challenges to overcome [13,15–18]. In comparison with photopolymerization, robocasting uses lower amounts of organic additives, which is an advantage as it avoids cracks and large shrinkages during the burnout and the sintering steps of bulk ceramic parts [19–21].

The fabrication of Si_3N_4-based ceramics by robocasting has been already explored in the literature but it is yet scarce and highly focused on lattice structures or porous devices, such as scaffolds for biomedical applications [18,22,23]. The mechanical integrity of the components obtained by this technology relies on the rheological properties of the feedstock [22]. Inks with shear thinning behavior and high elastic moduli are needed to guarantee simultaneously a proper flow through fine printing nozzles and filament shape retention just after printing, as well as to assure weight support of the subsequent layers. Zhao S. et al. [18] reported the ability to fabricate Si_3N_4 ceramics by robocasting using a mixture of low and high molecular weight polyethylene imine (PEI) and hydroxypropyl methylcellulose (HPMC) as binders in a paste containing around 62 wt% of solids (Si_3N_4 and Al_2O_3/Y_2O_3 as sintering aids). Almost fully dense Si_3N_4 samples with flexural strength of 552 ± 68 MPa were obtained by using HIP after sintering. Recently, Deiner et al. [24] published on the influence of using different printing patterns in residual porosity of Si_3N_4 components produced by DIW. The authors concluded that the print infill pattern (aligned, hexagonal, diagonal) affected the amount, size, and shape of pores in the final components. The maximum relative density reported was 97% for a feedstock paste containing 43.8 vol% of solids. In addition to porosity, fast drying and bending of the parts during the drying step were underlined as important themes to explore and control in this technology.

The present work aims to develop proper aqueous-based Si_3N_4 pastes as feedstock for robocasting and fine-tune their rheological properties. The influence of solids loading and cold isostatic pressing (CIP) as a post processing step in density and mechanical performance of the printed parts after pressureless sintering were studied and related with microstructural features.

2. Experimental procedure

2.1. Silicon nitride-based powder composition

Silicon nitride (Si_3N_4, Grade M11, H.C Starck, Germany), aluminum oxide (Al_2O_3, Martoxid MR 70, Huber Martinswerk, Germany) and yttrium oxide (Y_2O_3, ST-1028/98. H.C Starck, Germany), in a proportion of 89.3 wt%, 3.7 wt% and 7.0 wt%, respectively, were used as a powder-based composition, referred previously in literature as a proper combination to attain high densification levels [7]. To obtain a homogeneous distribution of all components, the powders' mixture was milled in a planetary milling (P400, Retsch, Portugal) for 8 h at 200 rpm in 2-propanol and then dried for 24 h, followed by calcination at 600 °C for 4 h, according to previous well-established procedures [25–28]. This powder composition was hereafter defined as A-matrix. The particle size distribution of the three ceramic powders and the final mixture was analyzed by a light-scattering instrument (Particle Size Analyzer, Coulter LS 230, UK).

Table 1
Detailed composition of the suspensions, added additives and final composition of the studied inks. The columns nomenclature is a reference to the solid loading (e.g. susp. 40%) of the pristine suspensions, which were partially diluted during the ink preparation process.

		Raw materials [wt. %]		Susp. 40 [vol %]	Susp. 42 [vol %]	Susp. 44 [vol %]
Suspensions	Solvent	Water		59.72	57.71	55.7
	A-Matrix	Si_3N_4	89.3%	40	42	44
		Y_2O_3	7%			
		Al_2O_3	3.7%			
	Dispersant	Dolapix A88		0.28	0.29	0.30
Rheology modifiers				**Amount of additives [wt. %]**		
	CMC solution	CMC-250	3%	8.72	9.15	8.59
		Water	97%			
		Polyethyleneimine (PEI)		0.07 (6)	0.08	0.08 (4)
Final inks/ pastes	**Constituents**			**Ink 36 [vol %]**	**Ink 38 [vol %]**	**Ink 39 [vol %]**
	Solvent			55.68	53.31	51.93
	A-matrix			36	38	39
	Dispersant			0.25	0.26	0.28
	CMC solution			7.99	8.35	8.72
	PEI			0.07	0.07 (3)	0.07 (6)

2.2. Feedstock preparation and characterization

Dolapix A88 and Dolapix PC33 (both from Zschimmer & Schwarz, Germany) respectively, an organic deflocculating agent (amino alcohol) free from alkali and a high-molecular-weight polyelectrolyte with carboxylic functional groups, were selected as dispersants, referred in literature as particularly effective in colloidal dispersion of silicon nitride [24,25,29]. The deagglomeration efficiency was evaluated by testing the impact promoted by different amounts of Dolapix A88 (0.1, 0.2, 0.3 and 0.4 wt%, based on total solids content) and Dolapix PC 33 (0.2, 0.4 and 0.8 wt%, based on total solids content), on the viscosity of an A-matrix-based suspension containing 40 vol%. To ensure the proper stability of the slurries, carboxymethyl cellulose (CMC, 250 000 Mw, Colorobia) was added to the suspensions as a binder/thickening agent. The suspensions were characterized by rheological properties using a rotational rheometer (Kinexus Pro+, Netzsch, Germany). Viscosity *versus* shear rate measurements were evaluated in the shear rate range of 0.1–100 s^{-1}, using a cone–plate system (4°/40 mm) with 150 μm gap. All measurements were assessed at room temperature (25 °C), holding a solvent trap to prevent samples drying during the experiments.

By using the dispersant selected and respective amount (Dolapix A88, 0.2 wt%) aqueous-based suspensions containing total solids loading in the range of 40–44 vol% were then prepared. For that, the A-matrix was gradually added to the aqueous media containing the dispersant and, the resultant suspension deagglomerated in a role milling with silicon nitride spheres for 24 h, to assure a complete homogenization and deflocculation. To reach the printable inks, a 3 wt% diluted solution of carboxymethyl cellulose was added to the previous suspension, using a planetary centrifugal mixer (ARE-250, Thinky Co., Tokyo, Japan) during 2 min at 650 rpm. Finally, polyethyleneimine solution (PEI, Sigma-Aldrich-Merck, Germany, Mn ~1800 and Mw ~2000), was

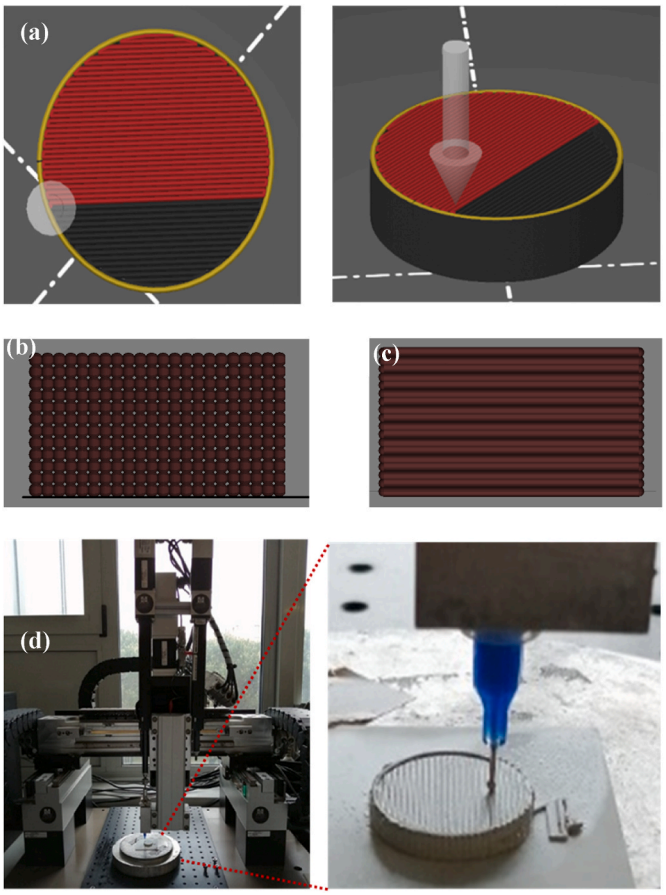

Fig. 1. CAD model of cylindrical samples and infill patterning used: (**a-c**) orthographic projections and (**d**) robocasting printing process of A-matrix based paste.

gradually added until a gel-like behavior is obtained and mixed followed by homogenization at 700 rpm for 2 min in the planetary mixer, attaining a 0.06 wt% (based on solid amounts) of this additive. The powder was added stepwise, by adding ~2–5 g at each step and the suspension was left on the planetary centrifugal mixer (ARE-250, Thinky Co., Tokyo, Japan) in steps of 2 min at 650 rpm. Since the tendency for agglomeration was dependent on the solid load, for the highest concentration suspensions, high number of steps adding small amounts of powder were needed, especially for the addition of the last quantities of powder, since the suspensions presented at this point an accentuated shear thickening behavior. Table 1 presents the (i) detailed composition of the suspensions, (ii) the amounts of rheology modifiers added in the previous suspensions to attain the ink and (iii) the final ink composition.

The zeta potential of the A-Matrix particles dispersed in water was determined using a Zeta-Sizer Nano ZS (Malvern, UK) equipment which operates according to the electrophoretic light scattering technique. The measurements were carried out as a function of the pH, changed by adding dropwise 0.1 M HCl or NaOH stock solutions, in the absence and in the presence of the dispersant previously determined as the most suitable (Dolapix A88). Likewise, the zeta potential of the A-Matrix particles in presence of Dolapix A88 and PEI was assessed. The final inks were characterized by their rheological behavior in oscillatory mode, using a plate sensor (Ø = 20 mm) with 1.5 mm gap size by amplitude sweep and frequency sweep measurements, respectively, at 1 Hz frequency and 50 Pa shear stress (from linear viscoelastic region, LVER).

2.3. Printing silicon nitride-based samples by direct ink writing and sintering

A robocasting equipment (EBDR-A32, 3D Inks, LLC, USA) was used to print cylindrical samples with 20 mm diameter and 5 mm thickness. For that, the A-Matrix ink was loaded into a 5 ml syringe (Nordson, Westlake, OH, USA) right after the homogenization. The ink extrusion was made at room temperature, with a print velocity of 10 mm/s through a nozzle with an internal diameter of 410 μm. The layer height was 322 μm. The samples were printed in an alumina substrate, in a high humidity environment to reduce the fast-drying effect of this type of pastes [30]. Fig. 1 (**a, b** and **c**) presents the CAD model with the infill patterning used, i.e., all layers with filament printed in the same direction and superimposed, already sustained by other authors [19]. An example of the robocasting printing process is presented on Fig. 1 (d). After printing, the samples were dried in a controlled humidity oven for 24 h and another 24 h at room temperature.

In order to reduce the porosity in green state and evaluate its effect in the final properties, some of the samples were submitted to cold isostatic pressing (CIP) for 15 min at 200 MPa (Autoclave Engineers, Erie, PA). This technique has been recently demonstrated to improve the mechanical properties of AM parts [31]. The samples were measured and weighted before and after CIP to determine the relative density. After that, the *de-binding* cycle was defined as 1 °C/min until 500 °C during 1 h (in air) at this temperature, with natural cooling. The printed samples were then placed inside a powder-bed composed by 50 wt% boron nitride (BN) + 50 wt% of starting powder, i.e. the A-Matrix powder [5,7,32,33]. This procedure derives from established practices at our lab to ensure low volatilization of matter and reduction of Si_3N_4 in the samples. The sintering process was carried out in a graphite furnace (Termolab, Águeda, Portugal) with a controlled N_2 atmosphere, slightly

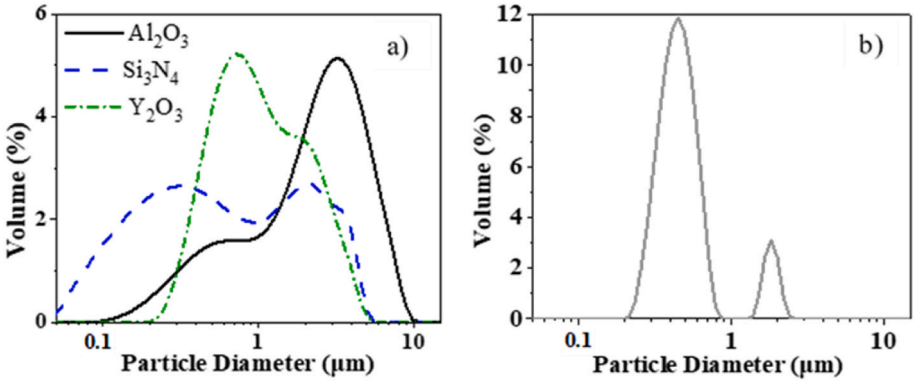

Fig. 2. Particle size distribution of **(a)** raw-materials (silicon nitride: Si_3N_4, alumina: Al_2O_3 and Yttria: Y_2O_3) and **(b)** A-matrix composition after milling step, containing 89.3 wt% Si_3N_4, 3.7 wt% Al_2O_3 and 7.0 wt% Y_2O_3. (For interpretation of the references to colour in this figure legend, the reader is referred to the Web version of this article.)

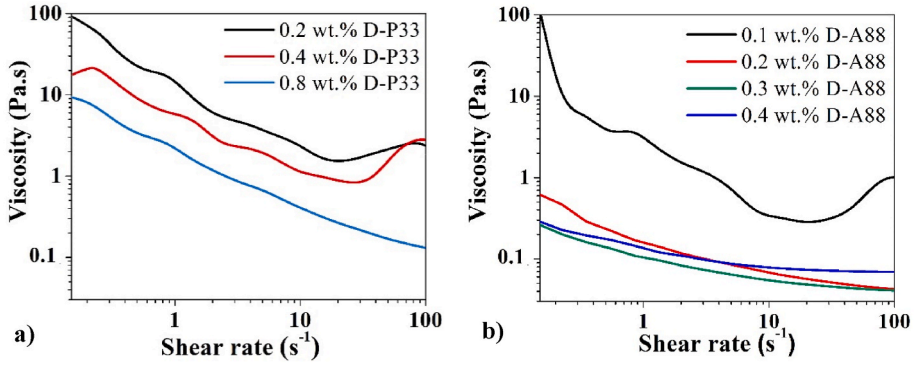

Fig. 3. Viscosity versus shear rate of A-matrix suspensions with 40 vol% solids in presence of **(a)** 0.2, 0.3 and 0.4 wt% Dolapix PC 33 (D-PC33) and **(b)** 0.1, 0.2, 0.3 and 0.4 wt% Dolapix A88 (D-A88).

above atmospheric pressure, at 1750 °C during 2 h [34]. The heating and cooling rates were 10 °C/min.

2.4. Characterization of printed Si_3N_4-based samples

The printed and sintered samples fabricated by robocasting, with and without CIP, were characterized in terms of structural and mechanical performance. The bulk density was calculated following the protocol of Archimedes immersion method. The analysis of the crystalline phases presented on the starting mixture and on the sintered samples were performed by X-ray diffraction (PANalyticalX'pert pro, Netherlands), using Cu-Kα radiation (λ = 1.5406 Å), in the 2θ range of 20° to 70°, angular step of 0.01° and a counting time of 100 s. The crystalline phases were identified by comparing the obtained diffractograms with patterns reported on the ICDD database, using the X'pert Highscore plus (PANalytical, Netherlands) software. Also, using the crystallographic data of the selected patterns, a quantitative phase analysis was performed based on the Rietveld refinement method [35].

A SiC abrasive paper sequence of P120–P180–P320–P600–P1000–P2500 (Carbimet, Buehler, Germany) was used for polishing and it was finished with a MD-Plan polyester plate (Struers, Denmark) and colloidal silica suspension, in an automatic polisher (LaboPress-3, Struers, Denmark). The microstructure of fractured samples, polished, and etched by CF_4 plasma, was examined by scanning electron microscopy (SEM, Hitachi SU70, Tokyo, Japan). The measurement of β-Si_3N_4 grains aspect ratio and size distribution, as well as the pore size distribution, was done using an open-source software for image processing (Image J - National Institute of Mental Health, USA) [36].

Vickers micro-hardness was measured in polished surfaces of the printed samples using 2 kgf, during 10 s in a Wilson VH1102 microhardness tester (Buehler, Illinois USA). An average of 12 measurements on each sample composition was gathered. Another set of 10 rectified and polished samples (discs of 1.2 ± 0.2 mm thick and a radius, R, of 7.7 ± 0.2 mm was submitted to a flexural strength test using the piston-on-three-ball (P–3B), at the constant rate of applied load of 1 mm/min according to ISO 6872 (2015) [37]. This methodology has been used for several authors for advanced ceramics due to the simple circular geometry required on the standard [38–41]. The testing device consists in a piston and a base with three symmetrically placed high hardness steel spheres spaced 120° apart. The bottom surface of the disc-shaped specimen's is supported by the spheres. The effects of friction between the supporting spheres and the bottom of the disc-shaped specimens were lessened by using a thin plastic sheet. The maximum flexural strength σ_f (MPa) was calculated using Equation (1):

$$\sigma_f = -\frac{0.2387F(X-Y)}{b^2} \quad (1)$$

where

$$X = (1+\nu)ln\,(r_2/r_3)^2 + [(1-\nu)/2](r_2/r_3)^2 \quad (2)$$

and

$$Y = (1+\nu)\left[1+ln\,(r_1/r_3)^2\right] + (1-\nu)(r_1/r_3)^2 \quad (3)$$

In Eqs (1)–(3) F is the rupture load (N), b is the specimen thickness (mm), r_1 is the radius of the supporting circle (mm), r_2 is the radius of the loaded area (mm), r_3 is the sample radius (mm) and ν is the measured Poisson ratio equal to 0.25 (as suggested by ISO 6872).

3. Results

3.1. Raw materials and feedstock characterization for direct ink writing (DIW)

Figure (a) and **(b)** present the particle size distribution of raw materials (Si_3N_4, Al_2O_3 and Y_2O_3) and the A-matrix composition after-milling, respectively. Silicon nitride powder has two particle populations centered around 0.3 μm and 2 μm, the latter probably due to agglomeration, with a D_{50} of 1.13 μm, while yttria presents a D_{50} of 1.34 μm. Alumina is the raw materials powder that presents the largest particle sizes with a D_{50} of around 2.8 μm.

After mixture and ball milling, the A-matrix composition presents the most representative particles' population with sizes less than 1 μm (centered around 0.5 μm), emphasizing the milling effectiveness of this operation. A small particles' population centered at ≈ 3 μm is less representative and could be resultant of the larger alumina particles or agglomeration of some fine particles.

The pastes' preparation for robocasting started with the selection of the most appropriate dispersant to obtain aqueous suspensions with a high solid loading which has the lowest viscosity as possible. Fig. 3 presents the viscosity *versus* shear rate for A-matrix suspensions in the presence of different amounts of Dolapix PC 33 and Dolapix A 88, containing a total of 40 vol% of solids.

The suspensions containing 0.2 and 0.4 wt% of Dolapix PC 33 present an accentuated shear thickening behavior at shear rate values higher than 50 s^{-1}, that tends to disappear when 0.8 wt% of Dolapix PC33 is added [30]. This shear thickening behavior for higher shear rate values is also visible in the suspension containing 0.1 wt% of Dolapix A88. For higher amounts of Dolapix A88 (0.2, 0.3 and 0.4 wt%) all suspensions exhibit a shear thinning behavior for all ranges of shear rates tested. Moreover, Dolapix A88 confers lower viscosity with lower added quantities when compared to Dolapix PC33. Similar viscosities are attained for suspensions with 0.2 and 0.3 wt% of Dolapix A88 at low shear rates that slightly increase for 0.4 wt%. According to these results, 0.2 wt% of Dolapix A88 was selected for further studies.

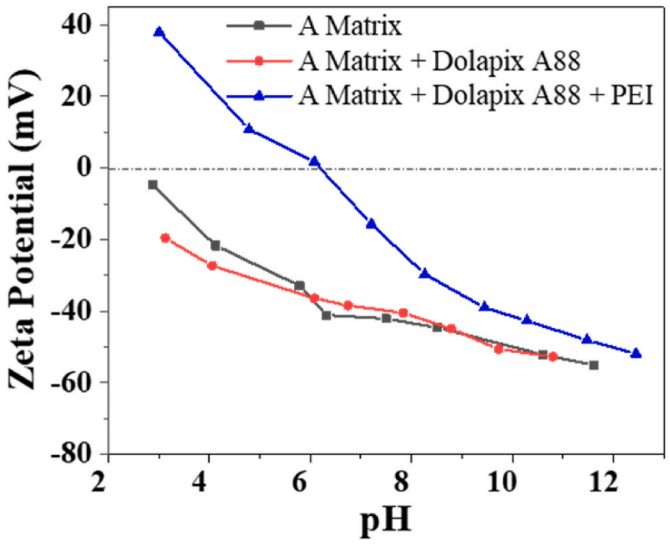

Fig. 4. Zeta Potential of A-matrix particles in absence and in presence of Dolapix A88 and PEI, as function of pH.

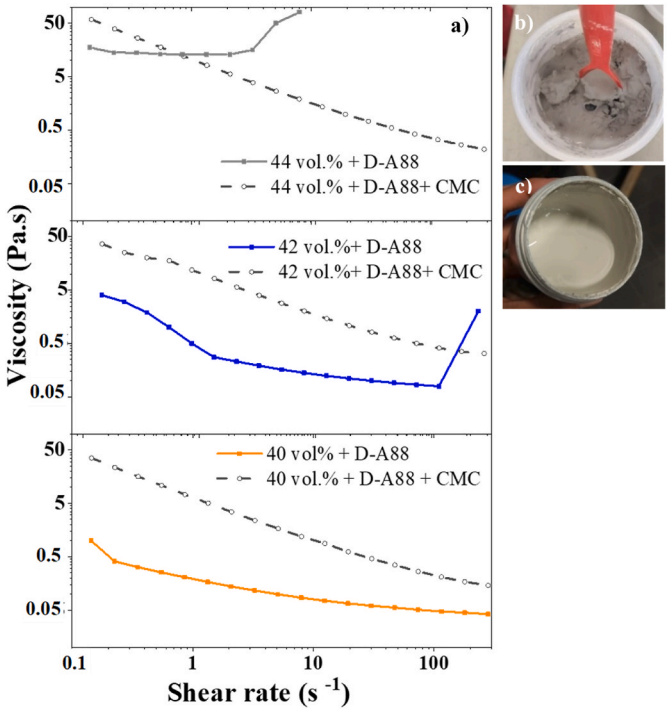

Fig. 5. (a) Flow curves of the A-matrix suspensions containing 40, 42 and 44 vol% of solids in the presence of 0.2 wt% Dolapix A88, without and with carboxymethyl cellulose (CMC), **(b)** example of a suspension with 44 vol% with a shear thickening behavior and **(c)** same suspension after CMC addition with shear thinning behavior.

The zeta potential of the A-Matrix suspension as a function of pH, in absence and in presence of Dolapix A88 is shown in Fig. 4. The A-matrix presents an isoelectric point (IEP) at pH values around 2–3, lower than IEP reported on the literature for a similar composition [42]. The addition of Dolapix A-88 does not contribute substantially for the modification of particles' surface charges, once the zeta potential results are not significantly altered, in good agreement with Seftel et al. [43]. The addition of PEI clearly promoted a dislocation of the IEP for more basic values (~6 pH).

Fig. 5 (a) presents the flow curves of the A-matrix suspensions containing 40, 42 and 44 vol%, with 0.2 wt% of Dolapix A88, before and after CMC addition. In the absence of CMC, suspensions with 42 and 44 vol% of solids presented a shear thickening behavior for high shear rate values, highly pronounced for 44 vol%. In fact, the suspensions only with dispersant at low shear rates appears to be shear thinning, but after a certain stirring, the suspension offers a considerable resistance, behaving like a solid (Fig. 5b). The addition of CMC confers to all suspensions a shear thinning behavior and an increase in the viscosity (Fig. 5c), even if the solids concentration decreased (as presented in Table 1).

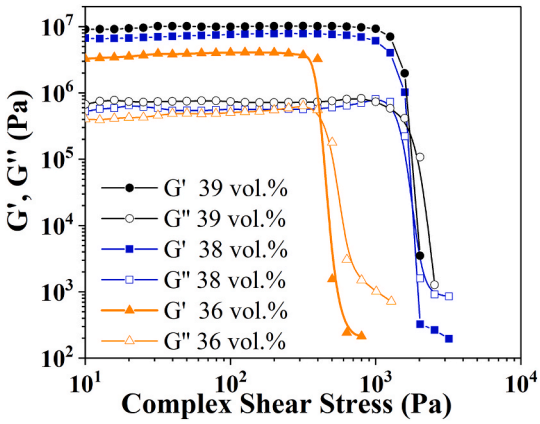

Fig. 6. Storage modulus (G′) and loss modulus (G″) *versus* shear stress for A-matrix pastes containing different amounts of solids (36, 38 and 39 vol%).

The rheological properties of the final inks are presented in Figs. 6 and 7 with amplitude sweep and frequency sweep measurements, respectively. For all A-matrix pastes from different concentrated suspensions, the elastic behavior (G′) dominates over the viscous one (G″) predominating a solid-like behavior without significative changes for pastes with different solids loading. The G' stability along a high shear stress range (linear viscoelastic region, LEVR) suggests that deposited paste rods will support the weight of subsequent layers during the printing process, keeping the mechanical integrity of the ceramic part.

The viscoelastic spectrum of the pastes was recorded by frequency sweep (Fig. 7). At low frequency values, G″ tends to be similar or somewhat higher than G′ for the A-matrix pastes with 36 and 38 vol% of solids, meaning that liquid-like behavior could predominate in rest conditions if given necessary time (Fig. 7a). This behavior is also perceptible by the complex modulus (G*) that decreases as frequency decreases, indicating a small stiffness at lower frequencies (Fig. 7b). For higher frequencies, a solid-like behavior and high stiffness is visible for all pastes. The highest concentrated paste (39 vol%) presents almost stable values of G' for all frequency values, characteristic of a solid-like system. The stiffness of the pastes given by the complex modulus (G*) is higher for the paste with the highest solids loading, in agreement with previous results. All the pastes presented a decrease in complex shear viscosity as frequency increases, as an indication of a shear thinning behavior, desirable for the extrusion-based printing process.

Additionally, during the printing process it was perceptible that the printed parts tend to dry very fast. This effect is highly pronounced for the pastes containing the highest solids loading in good agreement with concerns from other authors [44,45]. The option of using an oil bath to avoid high drying rates was not taken into account, since the literature mentioned that oil can be trapped between the filaments leading to void formation after burnout [19]. So, in order to prevent nozzle clogging and cracks in the printed parts, it was crucial to maintain a high humidity environment during the printing step, as well as a very slow drying process before the CIP and the heating treatments.

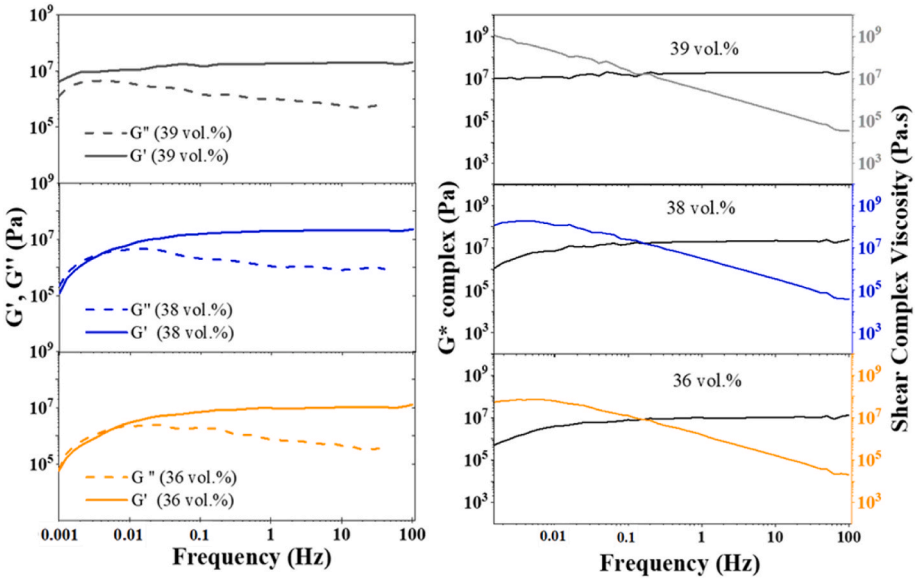

Fig. 7. Frequency sweep results for A-matrix pastes containing different amounts of solids (36, 38 and 39 vol%): **(a)** Storage modulus and loss modulus versus frequency and **(b)** complex modulus (G*) and complex shear viscosity versus frequency.

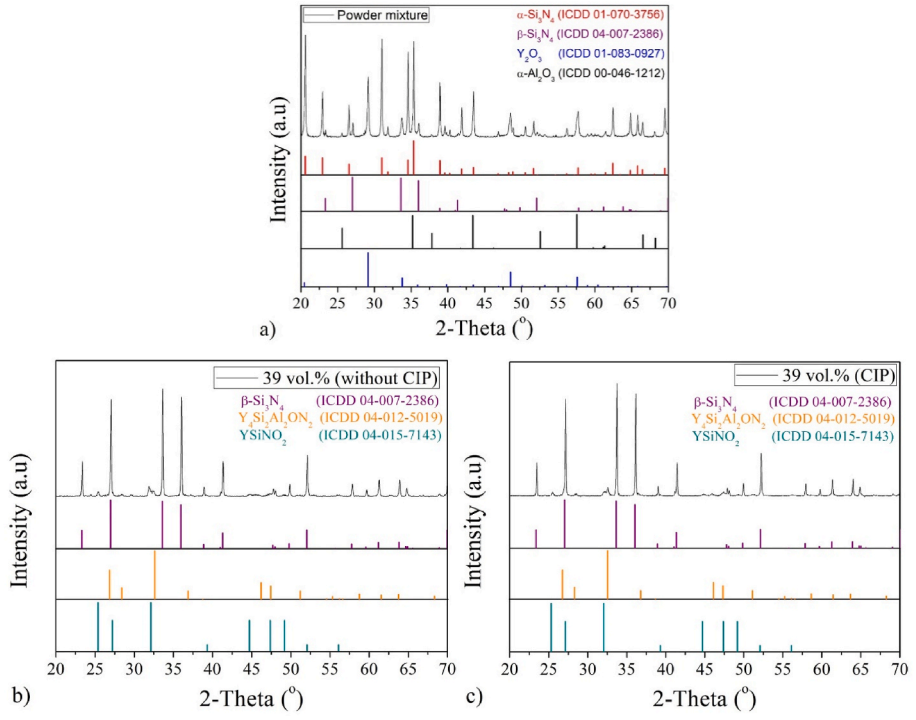

Fig. 8. X-ray diffraction profile of: **a)** A-Matrix powder mixture; **b)** printed and sintered 39 vol% sample; c) printed, CIPed and sintered 39 vol% sample.

3.2. Sintered Si_3N_4-based printed parts characterization

3.2.1. Crystalline phases

Fig. 8 shows the XRD spectrum of the raw materials' mixture and of the sintered samples with and without the CIP step. The silicon nitride powder used is mostly α-Si_3N_4 with some β- Si_3N_4 phase, as can be seen in Fig. 8a. Comparing the XRD spectrum of the sintered samples, Fig. 8b and c, it is clear that the α-Si_3N_4, Al_2O_3 and Y_2O_3 phases are no longer existing as individual phases. On the other hand, samples sintered with or without CIP presented β-Si_3N_4, oxynitride of yttrium aluminium silicon (Y–SiAlON), and oxynitride of yttrium silicon (Y–SiON), as crystalline phases.

The quantitative phase analysis supports that the measured phases ratio (82.1 wt% α-Si_3N_4, 7.5 wt% β-Si_3N_4, 7.1 wt% Y_2O_3 and 3.5 wt% Al_2O_3) on the starting powder mixture is in accordance with the desired composition. After sintering, samples processed with both conditions presented β-Si_3N_4 as the major phase (~90 wt%). However, the ratio between the secondary phases slightly changed for the samples processed with CIP (5.3 wt% Y–SiAlON and 3.9 wt% $YSiNO_2$) or without CIP (3.9 wt% Y–SiAlON and 5.9 wt% $YSiNO_2$). The crystallographic parameters measured by Rietveld refinement of the simulated models are presented in detail as supplementary data (Table S1 and Fig. S1).

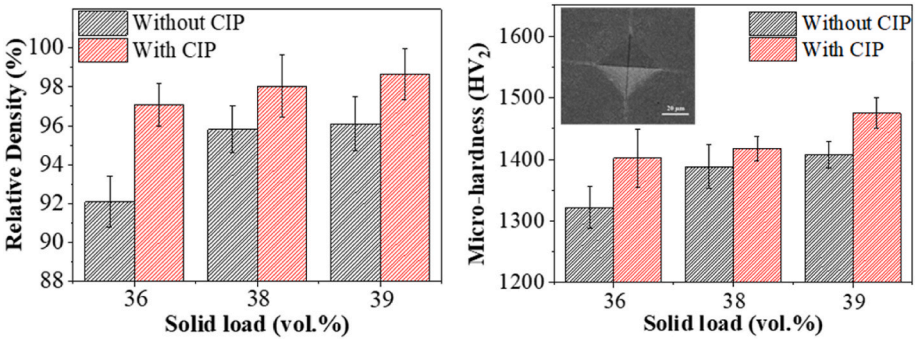

Fig. 9. relative density **(a)** and microhardness **(b)** of the printed Si_3N_4 parts obtained from the pastes with different amounts of solids loading (36, 38 and 39 vol%), without and with cold isostatic pressure (CIP) as post processing.

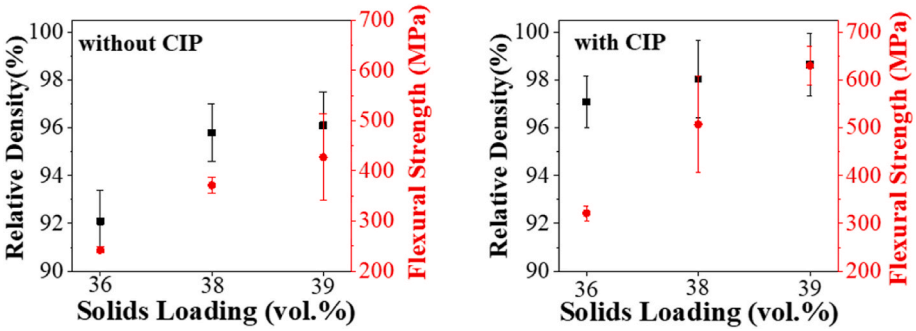

Fig. 10. Densification and Flexural strength results of sintered A-Matrix samples obtained from pastes with 36, 38 and 39 vol% of solids, without and with cold isostatic pressure (CIP) after printing.

3.2.2. Structural and mechanical properties

Fig. 9 shows the relative density and micro-hardness for each composition, with and without CIP as post-processing. It is possible to observe that CIP improves both properties of each solid load composition specimens. Also, both relative density and micro-hardness rises as the solid load in the sourced pastes increases. Relative density increases from an average of 92% for parts obtained with the paste having 36 vol% of solids to an average of 96% for the ones obtained with 39 vol% paste, in absence of CIP. Applying CIP, relative densities presented at least a 2% improvement for both parts obtained from 38 to 39 vol% pastes. The highest relative density improvement (around 5%) was observed for the parts produced from the paste with 36 vol% solids. The highest relative density, 98.6 ± 1.3% value was attained for the sample with 39 vol% solids submitted to CIP. Samples with the same solids loading, without CIP, have an average of 96 ± 1.4% relative density.

The average hardness of the samples obtained for 36, 38 and 39 vol% with CIP were 1402 (13.7 GPa), 1418 (13.9 GPa) and 1475 HV2 (14,5 GPa), while for the same compositions without CIP were 1322 (12.9 GPa), 1388(13.6 GPa) and 1407 HV2 (13.8 GPa).

The flexural strength results of all printed and sintered parts are presented in Fig. 10. For comparison purposes, relative density is also plotted in these graphs.

As it can be seen, flexural strength increases as solid loading in the sourced pastes increases, following the same trend as relative density. The CIPped parts obtained from the paste with the same solids loading, presents higher values of flexural strength, as expected. The average flexural strength of the 39 vol% samples with CIP was 630 ± 41.02 MPa while the same composition without CIP presents flexural strength values of 427.11 ± 86 MPa. It is important to mention that almost all results presented a high variability inherent to the printing process. In fact, samples made by AM have limited reproducibility caused by defects generated during the printing, such as missing layers, filament extrusion deficiency, cracks resultant of fast drying and poor green mechanical resistance. So, the flexural strength results could be clarified by analyzing the microstructure of the cross-section after the flexural test. Fig. 11 presents the fracture surface resulting from the flexural strength test of parts obtained from pastes with 39 vol%. Fig. 11 (a) and (b) refer to samples without CIP while Fig. 11 (c) are representative of a sample with CIP.

The samples processed without CIP fractured in a reduced number of parts, usually 2, as shown in Fig. 11 a) and **b)**. The probability of fracture origin in these samples are highlighted with red circles and could be identified as drying cracks, missing filaments, and interfilamentous pores. On the other hand, CIPed samples fractured on 3 or more parts, Fig. 11 c). In this case no macro-defects were visible. These fracture behaviors can be related with the material's intrinsic properties and the tensile stress distribution of the chosen flexural strength test.

The micrographs of the different samples with and without CIP are presented in Fig. 12. The microstructure shows long needle-shaped β-Si_3N_4 crystals embedded in the Y–Al–O matrix containing intergranular, partially recrystallized, glassy phase, in accordance with a similar material obtained using conventional processing methods [46].

4. Discussion

Si_3N_4 suspensions presented a pronounced shear thickening behavior that is reverted to a shear thinning behavior thanks to the addition of the correct amount of dispersant, being Dolapix A-88 the one that results in low viscosity values (Fig. 3). However, the shear thickening behavior is intensified as solids loading increases, even for the optimized amount of Dolapix A-88. According to literature, several mechanisms could explain the shear thickening phenomenon, including interparticle interactions and particle interlocking [47,48]. Then, small particle sizes, narrow particle size distribution (Fig. 2) and solid volume fraction close to the critical value, promoting the frictional contacts between particles (Fig. 3), could explain the shear thickening in Si_3N_4 suspensions [48]. In

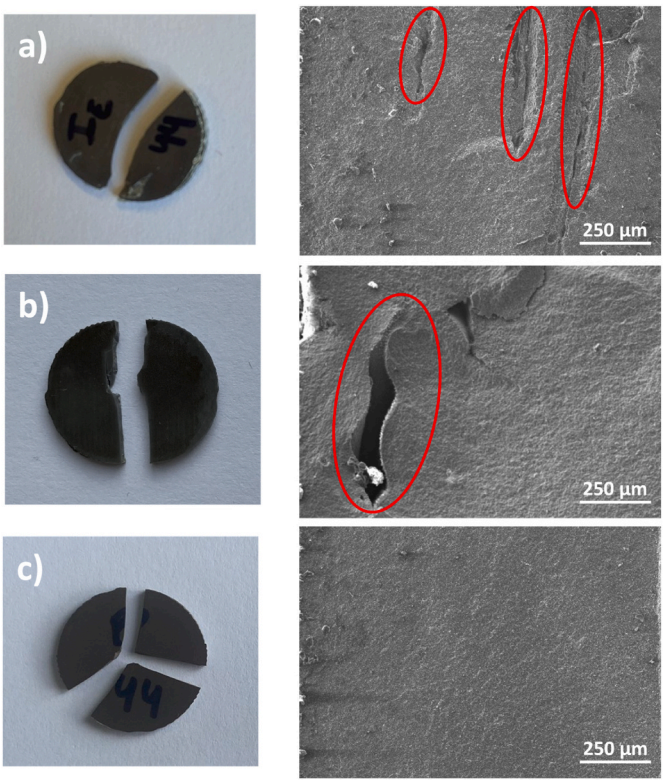

Fig. 11. Surface fracture of samples with 39 vol%, resulting from the flexural strength test. Samples a) and b) were sintered as printed (without CIP) while sample c) was CIPed after printing. Probable fracture origins are stressed with red circles, a) drying cracks and b) printing pattern. (For interpretation of the references to colour in this figure legend, the reader is referred to the Web version of this article.)

fact, this behavior is typical for Si_3N_4 suspensions and also mentioned by other reports [49], which could explain the difficulties in exploring suspension-based AM technologies in the Si_3N_4 fabrication.

The heat treatment at 600 °C of the Si_3N_4 powder enhances the presence of silanol (Si–OH) with consequent reduction of amina groups (=N–H) at the particles 'surface, explaining the dislocation of the IEP for more acidic region (Fig. 4) when compared with the results in other studies [42]. The low impact of Dolapix A-88 addition in the zeta potential (Fig. 4) of A-matrix can be related with its adsorption mechanism. Since this dispersant is a 2-amino-2 methyl propanol, the adsorption can be promoted by chemical interactions between its polymer chain and broken chemical bonds on the surface of the Si_3N_4 particles, e.g. SiO^- or Si_2N^-, through the concomitant formation of SiOH or $SiNH_2$ [29]. Another possibility is that the polymer chain of the dispersant is adsorbed only physically in nature [43]. Therefore, in both possibilities, the addition of Dolapix A88 would not lead to substantial variations on the zeta potential. Consequently, the viscosity reduction verified on the A-matrix suspensions in presence of this dispersant is possibly strongly related to a steric stabilization mechanism. Also, the dispersant adsorbed on the ceramic particles can act as a free surface for the adhesion of CMC. As CMC has a higher molecular weight than the dispersant, it intensifies the steric rheological stabilization process, that helps their alignment under flow conditions [50] and effectively eliminates the shear thickening behavior (Fig. 5). The dilution effect (solids loading reduction) conferred by the CMC addition in the suspensions could also promote a shear thinning behavior. Subsequently, PEI acts as a coagulating agent by charge neutralization. The combination of CMC and PEI resulted in Si_3N_4 inks with the proper shear thinning, viscoelastic and yield stress values adequate for the printing process (Figs. 6 and 7).

The thermal post-processing of the printed parts also presents a challenge, due to the strong covalent structure of Si_3N_4 and its relatively low decomposition temperature (~1800 °C). During sintering, the oxides (alumina and yttria) react with the SiO_2 present as an oxidation layer on the surface of the Si_3N_4 particles, producing a liquid phase with an eutectic temperature of about 1550 °C (for the A-matrix composition) that aids in the rearranging of the Si_3N_4 particles in the initial stages of densification [7]. The α-Si_3N_4 grains are then also dissolved into this liquid, at higher temperatures and for longer times, reprecipitating as the more stable β- Si_3N_4 phase, presented in the final microstructure. Upon cooling the liquid phase may appear as an amorphous glassy phase or may recrystallize totally or partially. The XRD pattern (Fig. 8b) clearly shows that at least some of the liquid phase recrystallized as an oxynitride of yttrium aluminium silicon-so called Y–SiAlON - and as an oxynitride of yttrium silicon (Y–SiON) [32,51–53]. This is valid also for the samples sintered after the CIP step, although with a slight modification in the amount of these phases, as the XRD pattern in Fig. 8c seems to indicate. The relative intensity of the maximum peak of Y–SiON and of Y–SiAlON are reversed: the first is more intense in samples without CIP while the latter is more intense for samples processed by CIP. The Rietveld analysis performed on the XRD of both types of samples corroborates quantitatively these findings. This is most likely a consequence of a more intimate contact between the reagents during heating in CIPed samples, resulting in faster and more complete reactions that altered the composition of the liquid phase in the later stages of densification. Also, there is no significant oxidation due to the absence of amorphous silica phase (Fig. S1 in Supplementary information).

The microstructural data (Fig. 12) agrees with the densification mechanisms previously discussed. Following a solution-diffusion-precipitation process, a β-Si_3N_4 phase tends to be grow from the oxynitride liquid phase. Due to a preferential diffusion direction along the c-axes, the β-Si_3N_4 crystals usually grow with an elongated shape, presenting a prismatic habit. Consequently, despite the processing conditions, all samples presented a matrix based on interlocked prismatic crystals of high aspect ratio, characteristic of the β-Si_3N_4 phase, surrounded by a brighter structure, related with the Y–SiON and Y–SiAlON phases and, assumedly, remains of the glassy phase. On the other hand, the minor phases seem to be homogeneously distributed all over the microstructure, involving the β-Si_3N_4 crystals. Also, the mismatch between the Young's modulus and the coefficient of thermal expansion of the minor phases and the β-Si_3N_4 is reportedly low [54,55]. Thus, it avoids the induction of undesired thermal residual stresses, inhibiting microcracking during cooling and improving the final density.

As stated in other works, the relative density was directly connected to the rheological properties of the inks and printing parameters, as well as to the post-processing [19,24]. Regardless of the solids loading, relative density of the sintered samples submitted to the CIP process, is higher than those who were sintered without CIP (Fig. 9). In fact, this improvement is also related to the green densities of the samples that presented relative densities around 49.4% (after drying) and 57.46%, without and with CIP, respectively. The close connection between the powder particles, higher in CIPed samples, is helpful to increase the number of contact points, a key parameter for the action of the densification mechanisms during sintering. Consequently, the average pore size on samples submitted to the CIP process is smaller (0.78 μm ± 0.09) than that of the samples which were sintered as printed (0.95 μm ± 0.24), additionally the pore population is clearly reduced, as show in Fig. 13. However, as previously reported for conventional preforming techniques, it was observed here that bigger internal defects are difficult to eliminate, resulting in dimples on the surface of the CIP processed sample. This is especially useful to discard the defective samples in earlier stage, before the sintering step. Consequently, the analyzed CIP-treated samples are less likely to present macroscopic defects.

These results agree with the micro-hardness values (Fig. 8b), i.e. samples based on an ink of higher solids loading, and processed with CIP, present better densification, smaller pores, and consequently higher hardness. This relationship between density and hardness is valid for all

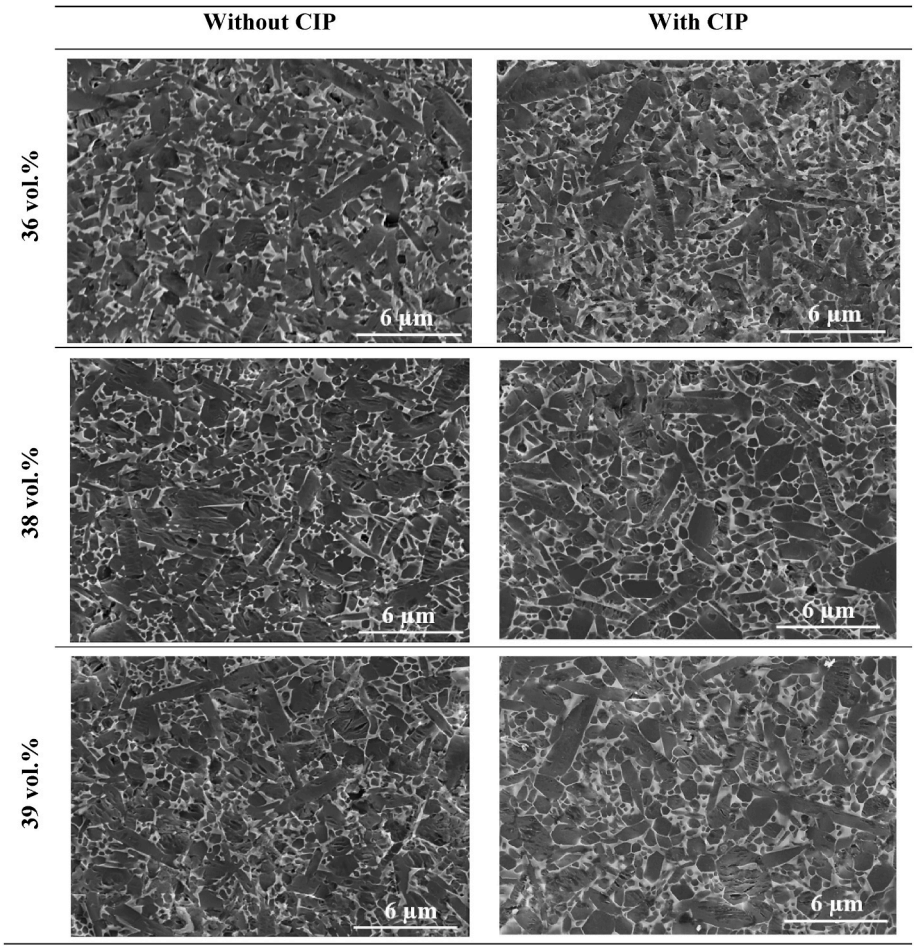

Fig. 12. SEM morphology of non-CIPed and CIPed sintered Si_3N_4 printed parts after plasma etching obtained with pastes containing different amounts of solids (36, 38 and 39 vol%).

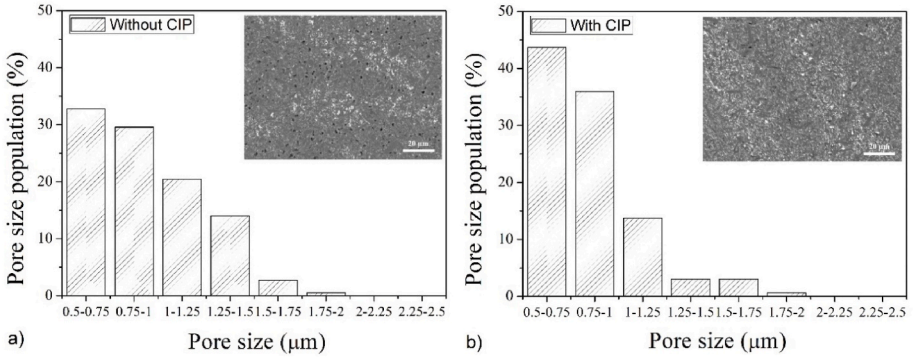

Fig. 13. Pore size population of polished surfaces (cross-section) of 39 vol% sintered sample with and without cold isostatic pressure (CIP) as post processing.

materials [56]. Nonetheless, adding CIP as post-processing, the hardness values were expressively improved, achieving comparable values to the conventional processed Si_3N_4-ceramics parts (such as uniaxial pressing ones) [7,57].

In the same way, the flexural strength behavior is directly related to the density (Figs. 9 and 10), crystalline phases (Fig. 8) and microstructural features (Figs. 11 and 12). According to the literature, in the piston on three balls flexural strength test, the maximum tensile stress regions are around the contact points between the sample and the three spheres [58]. Consequently, it is expectable that the material fracture occurs on these regions, leading to a standard fracture being in three parts. On the other hand, the presence of flaws on the material volume will induce the existence of stress concentrators in regions of the sample that are not supposed to experience maximum stress, which can induce unexpected fracture behaviors.

A well accepted explanation for the influence promoted by the flaw size on the fracture criterion is the Griffith theory, Equation (4). This classic theory of fracture mechanics for brittle materials proposes a correlation between the maximum stress of failure (σ_c) with the materials stress intensity factor (K_{IC}), e.g fracture toughness, a dimensionless geometric factor (γ) and the critical flaw size (a_c).

Table 2
Characteristics of Si_3N_4 ceramics using different AM processes. Comparison between literature results and results attained in the present work.

Ref.	Solids load (vol%)	Processing technology	Sintering method	Relative density (%)	Flexural strength (MPa)	Vickers Hardness (HV)
[63]	40	LOM	HIP 1800 °C 35 MPa 0.5 h	99.0	725	–
			SPS 1600 °C 30 MPa 3 min	98.1	650	–
[62]	48.7	LOM	Conventional 1800 °C - 1 h	94.3	475	–
[20]	40	SLA	Conventional 1800 °C - 4 h	99.8	764	1500 HV_{10}
[65]	45	SLA	Conventional 1750 °C - 2 h	95.0	–	1463 HV_{10}
[51]	35	DLP	Conventional 1800 °C - 2 h	85.0	150	–
[64]	32.5	IJP	Conventional 1780 °C - 2 h	96.0	–	1700 $HV_{0.2}$
[66]	35	DIW	HIP 1700 °C 200 MPa 2 h	99.0	552	–
[24]	43	DIW	1700 ° C- 3 h	98.0	–	–
[49]	40	DIW	1750 ° C- 2 h	98.4	348	–
This work	**39**	**DIW**	**Conventional 1750°C - 2 h**	**94.5–97.5**	**430**	**1407 HV_2**
This work	**39**	**DIW + CIP**	**Conventional 1750°C - 2 h**	**98–99**	**650**	**1475 HV_2**

Where: LOM: Laminate Object Manufacturing; SLA: Stereolithography; IJP: Inkjet Printing; DLP: Digital Light Processing; SLS: Selective Laser Sintering; DIW: Direct Ink Writing; HIP: Hot Isostatic Processing and SPS: Spark Plasma Sintering.

$$\sigma_c = \frac{K_{IC}}{\gamma\sqrt{a_c}} \quad (4)$$

This is in accordance with the fractographic analysis of the samples processed without CIP (Fig. 11). The observed printing defects (Fig. 11 a) and **b**), are far bigger than the reported critical flaw size for silicon nitride, which according to the literature is between 2 and 30 μm [59–61]. It is important to mention that printing defects (Fig. 11 a) and **b)**) are not solved by CIP. Macro defects in samples processed by CIP usually results in the fracture of the piece or on the development of big lumps; thus, it is unfeasible to sinter the sample. Consequently, most of these samples failed in 2 parts and with printing defects, or drying cracks, visible around the region of maximum tensile stress, the face turned down during the bending test. On the other hand, samples processed with CIP fractured in 3 or 4 parts, presented flat fracture surface, as the sample shown in Fig. 11 c), and a high stress tolerance, 943 N (676 MPa), before cracking. Some reports state an increase in the number of fractured parts, when the analyzed material presents toughening mechanisms. Since a tougher material will withstand higher fracture stresses, when the maximum stress is achieved the fracture tends to begin simultaneously in multiple regions of minor structural defects, leading to several crack paths at the same time.

In fact, the mechanical properties measured here can be considered highly comparable with others presented in the literature for additive manufacturing technologies, as resumed in Table 2. To the best of the authors knowledge, the values of flexural strength reported in the present work (650 MPa) with CIP as post-processing are higher than those presented by previous works related to the robocasting processing technology for Si_3N_4 (350–552 MPa) [18,24,49]. However, since the mechanical properties are usually related to multifactorial parameters, e.g. ink's properties, sintering additives, sintering procedure, the direct comparison between these data is not straightforward. Nevertheless, the better mechanical properties (650–725 MPa) are reported for Laminate Object Manufacturing (LOM) technology, when the samples are prepared by specific sintering methods, e.g. hot isostatic pressing, and spark plasma sintering [62,63]. On the other hand, for Si_3N_4 samples processed by light curing techniques (SLA/DLP) a high variability of flexural strength values (150–764 MPa) are reported from different authors [20,51,64]. Although these techniques could produce samples with better surface finishing, drawbacks related to the de-binding process are still an issue, compromising the final mechanical performance of bulk ceramic parts [20].

5. Conclusions

Robocasting was successfully used to print almost dense silicon nitride ceramics from pastes with 39 vol% maximum of solids, by using minimum amounts of additives (CMC and PEI). Suitable inks with required rheological properties for extrusion were developed, by eliminating the characteristic shear thickening behavior of silicon nitride suspensions. The use of cold isostatic pressing as a post processing was helpful to enhance the relative density and consequently the mechanical performance in all developed printed parts. High-density (>99%) samples were achieved with a maximum flexural strength of 676 MPa and a maximum micro-hardness (HV2) value of 14.5 GPa.

The results presented and discussed in this study represents a strong advance in the field of AM of silicon-nitride based ceramics and highlights the high potential of robocasting to fabricate technical ceramics for high demanding applications. The use of CIP improved the mechanical performance of simple geometries, opening the possibility to explore this technology for the processing of more geometrically complex structures.

Declaration of competing interest

The authors declare that they have no known competing financial interests or personal relationships that could have appeared to influence the work reported in this paper.

Acknowledgments

This work was developed within the scope of 3DCompCer project with reference number POCI-01-0247-FEDER-047060 funded by FEDER funds through the COMPETE 2020 Programme and National Funds through FCT - Portuguese Foundation for Science and Technology. The project CICECO-Aveiro Institute of Materials, UIDB/50011/2020, UIDP/50011/2020 & LA/P/0006/2020, financed by national funds through the FCT/MEC (PIDDAC) is also acknowledged. S M Olhero acknowledge FCT for CEECIND/03393/2017 contract. M.F.R.P. Alves acknowledges the FCT for the PhD grant (2021.06615.BD).

Appendix A. Supplementary data

Supplementary data to this article can be found online at https://doi.org/10.1016/j.ceramint.2023.03.231.

References

[1] M.H. Bocanegra-Bernal, B. Matovic, Dense and near-net-shape fabrication of Si3N4 ceramics, Mater. Sci. Eng., A 500 (1–2) (2009) 130–149, https://doi.org/10.1016/j.msea.2008.09.015.
[2] M. Zanocco, et al., 3D-additive deposition of an antibacterial and osteogenic silicon nitride coating on orthopaedic titanium substrate, J. Mech. Behav. Biomed. Mater. 103 (2020), 103557, https://doi.org/10.1016/j.jmbbm.2019.103557. November 2019.

[3] B. Baudrillart, F. Bénédic, A.S. Melouani, F.J. Oliveira, R.F. Silva, J. Achard, Low-temperature deposition of nanocrystalline diamond films on silicon nitride substrates using distributed antenna array PECVD system, Phys. Status Solidi Appl. Mater. Sci. 213 (10) (2016) 2575–2581, https://doi.org/10.1002/pssa.201600221.

[4] L. Wang, R.W. Snidle, L. Gu, Rolling contact silicon nitride bearing technology: a review of recent research, Wear 246 (1–2) (2000) 159–173, https://doi.org/10.1016/S0043-1648(00)00504-4.

[5] M.H. Bocanegra-Bernal, B. Matovic, Mechanical properties of silicon nitride-based ceramics and its use in structural applications at high temperatures, Mater. Sci. Eng., A 527 (6) (2010) 1314–1338, https://doi.org/10.1016/j.msea.2009.09.064.

[6] X. Lao, X. Xu, W. Jiang, J. Liang, L. Miao, G. Leng, Effects of various sintering additives on the properties of β-SiAlON–SiC ceramics obtained by liquid phase sintering, Ceram. Int. 47 (9) (2021) 13078–13092, https://doi.org/10.1016/j.ceramint.2021.01.172.

[7] J. Yang, F.J. Oliveira, R.F. Silva, J.M.F.F. Ferreira, Pressureless sinterability of slip cast silicon nitride bodies prepared from coprecipitation-coated powders, J. Eur. Ceram. Soc. 19 (4) (1999) 433–439, https://doi.org/10.1016/S0955-2219(98)00222-2.

[8] F. Çalişkan, Z. Tatli, A. Genson, S. Hampshire, Pressureless sintering of β-SiAlON ceramic compositions using fluorine and oxide additive system, J. Eur. Ceram. Soc. 32 (7) (2012) 1337–1342, https://doi.org/10.1016/j.jeurceramsoc.2011.05.016.

[9] A. Zocca, P. Colombo, C.M. Gomes, J. Günster, Additive manufacturing of ceramics: issues, potentialities, and opportunities, J. Am. Ceram. Soc. 98 (7) (2015) 1983–2001, https://doi.org/10.1111/jace.13700.

[10] S.A.M. Tofail, E.P. Koumoulos, A. Bandyopadhyay, S. Bose, L. O'Donoghue, C. Charitidis, Additive manufacturing: scientific and technological challenges, market uptake and opportunities, Mater. Today 21 (1) (2018) 22–37, https://doi.org/10.1016/j.mattod.2017.07.001.

[11] Z. Chen, et al., 3D printing of ceramics: a review, J. Eur. Ceram. Soc. 39 (4) (2019) 661–687, https://doi.org/10.1016/j.jeurceramsoc.2018.11.013.

[12] Y. Lakhdar, C. Tuck, J. Binner, A. Terry, R. Goodridge, Additive manufacturing of advanced ceramic materials, Prog. Mater. Sci. 116 (2021), 100736, https://doi.org/10.1016/j.pmatsci.2020.100736.

[13] T.G. Aguirre, C.L. Cramer, D.J. Mitchell, Review of additive manufacturing and densification techniques for the net- and near net-shaping of geometrically complex silicon nitride components, J. Eur. Ceram. Soc. 42 (3) (2022) 735–743, https://doi.org/10.1016/j.jeurceramsoc.2021.11.001.

[14] S.M. Olhero, P.M.C. Torres, J. Mesquita-Guimarães, J. Baltazar, J. Pinho-da-Cruz, S. Gouveia, Conventional versus additive manufacturing in the structural performance of dense alumina-zirconia ceramics: 20 years of research, challenges and future perspectives, J. Manuf. Process. 77 (2022) 838–879, https://doi.org/10.1016/j.jmapro.2022.02.041.

[15] X. Wu, C. Xu, Z. Zhang, Development and analysis of a high refractive index liquid phase Si3N4 slurry for mask stereolithography, Ceram. Int. 48 (1) (2022) 120–129, https://doi.org/10.1016/j.ceramint.2021.09.087.

[16] W. Zou, P. Yang, L. Lin, Y. Li, S. Wu, Improving cure performance of Si3N4 suspension with a high refractive index resin for stereolithography-based additive manufacturing, Ceram. Int. (2022), https://doi.org/10.1016/j.ceramint.2022.01.124.

[17] C.M. Clarkson, C. Wyckoff, M.J.S. Parvulescu, L.M. Rueschhoff, M.B. Dickerson, UV-assisted direct ink writing of Si3N4/SiC preceramic polymer suspensions, J. Eur. Ceram. Soc. 42 (8) (2022) 3374–3382, https://doi.org/10.1016/j.jeurceramsoc.2022.03.001.

[18] S. Zhao, W. Xiao, M.N. Rahaman, D. O'Brien, J.W. Seitz-Sampson, B. Sonny Bal, Robocasting of silicon nitride with controllable shape and architecture for biomedical applications, Int. J. Appl. Ceram. Technol. 14 (2) (2017) 117–127, https://doi.org/10.1111/ijac.12633.

[19] J. Baltazar, P.M.C. Torres, J. Dias-de-Oliveira, J. Pinho-da-Cruz, S. Gouveia, S. Olhero, Influence of filament patterning in structural properties of dense alumina ceramics printed by robocasting, J. Manuf. Process. 68 (2021) 569–582, https://doi.org/10.1016/j.jmapro.2021.05.043.

[20] A.A. Altun, T. Prochaska, T. Konegger, M. Schwentenwein, Dense, strong, and precise silicon nitride-based ceramic parts by lithography-based ceramic manufacturing, Appl. Sci. 10 (3) (2020), https://doi.org/10.3390/app10030996.

[21] Y. Liu, et al., Formation mechanism of stereolithography of Si3N4 slurry using silane coupling agent as modifier and dispersant, Ceram. Int. 46 (10) (2020) 14583–14590, https://doi.org/10.1016/j.ceramint.2020.02.258.

[22] L. del-Mazo-Barbara, M.P. Ginebra, Rheological characterisation of ceramic inks for 3D direct ink writing: a review, J. Eur. Ceram. Soc. 41 (16) (2021) 18–33, https://doi.org/10.1016/j.jeurceramsoc.2021.08.031.

[23] M.A. Sainz, S. Serena, M. Belmonte, P. Miranzo, M.I. Osendi, Protein adsorption and in vitro behavior of additively manufactured 3D-silicon nitride scaffolds intended for bone tissue engineering, Mater. Sci. Eng. C 115 (2020), 110734, https://doi.org/10.1016/j.msec.2020.110734.

[24] S. Diener, et al., X-ray microtomography investigations on the residual pore structure in silicon nitride bars manufactured by direct ink writing using different printing patterns, Open Ceram 5 (2021), 100042, https://doi.org/10.1016/j.oceram.2020.100042.

[25] M.I.L.L. Oliveira, K. Chen, J.M.F. Ferreira, Influence of powder pre-treatments on dispersion ability of aqueous silicon nitride-based suspensions, J. Eur. Ceram. Soc. 21 (13) (2001) 2413–2421, https://doi.org/10.1016/S0955-2219(01)00202-3.

[26] F.A. de Almeida, Nano to Micrometric Grain Sized CVD Diamond for Turning Hard and Abrasive Materials, University of Aveiro, 2007.

[27] J.M. Carrapichano, A. Taillaire, F.J. Oliveira, R.F. Silva, Complete densification of Si3N4 - SiC ceramic matrix composites (CMC's) by a pressureless sintering route, Mater. Sci. Forum 455 (456) (2004) 225–229. https://doi.org/10.4028/www.scientific.net/msf.455-456.225.

[28] S.S. Camargo, J.R. Gomes, J.M. Carrapichano, R.F. Silva, C.A. Achete, Silicon-incorporated diamond-like coatings for Si3N4 mechanical seals, Thin Solid Films 482 (1–2) (2005) 221–225, https://doi.org/10.1016/j.tsf.2004.11.149.

[29] B.P. Singh, S. Gaydardzhiev, P. Ay, Stabilization of aqueous silicon nitride suspension with Dolapix A88, J. Dispersion Sci. Technol. 27 (1) (2006) 91–97, https://doi.org/10.1081/DIS-200066756.

[30] Cesarano Joseph, Processing and Mechanical Properties of Silicon Nitride Formed by Robocasting Aqueous Slurries, 2000, https://doi.org/10.1002/9780470294635.ch72. New Mexico.

[31] K. Wang, R. Liu, H. Xu, High-strength and wave-transmitting Si3N4–Si2N2O-BN composites prepared using selective laser sintering, Ceram. Int. 48 (14) (2022) 20126–20133, https://doi.org/10.1016/j.ceramint.2022.03.291.

[32] H. Ma, C. Bao, Preparation, oxidation property and mechanism of Si3N4/O′-SiAlON composite ceramics, Ceram. Int. 47 (11) (2021) 15383–15391, https://doi.org/10.1016/j.ceramint.2021.02.103.

[33] P. Popper, Sintering of Silicon Nitride, a Review, Springer Netherlands, Dordrecht, 1983.

[34] M. Vila, J.M. Carrapichano, J.R. Gomes, S.S. Camargo, C.A. Achete, R.F. Silva, Ultra-high performance of DLC-coated Si3N4 rings for mechanical seals, Wear 265 (5–6) (2008) 940–944, https://doi.org/10.1016/j.wear.2008.01.007.

[35] R.J. Hill, C.J. Howard, Quantitative phase analysis from neutron powder diffraction data using the Rietveld method, J. Appl. Crystallogr. 20 (6) (1987) 467–474, https://doi.org/10.1107/S0021889887086199.

[36] M. Lau, et al., Image segmentation variants for semi-automated quantitative microstructural analysis with ImageJ, Prakt. Metallogr. Metallogr. 57 (11) (2020) 752–775, https://doi.org/10.3139/147.110626/machinereadablecitations/ris.

[37] ISO 6872, Dentistry-Ceramic Materials, 2015, p. 28.

[38] A. Hadian, M. Fricke, A. Liersch, F. Clemens, Material extrusion additive manufacturing of zirconia parts using powder injection molding feedstock compositions, Addit. Manuf. 57 (Sep) (2022), https://doi.org/10.1016/J.ADDMA.2022.102966.

[39] A. Zocca, P. Lima, S. Diener, N. Katsikis, J. Günster, Additive manufacturing of SiSiC by layerwise slurry deposition and binder jetting (LSD-print), J. Eur. Ceram. Soc. 39 (13) (Oct. 2019) 3527–3533, https://doi.org/10.1016/J.JEURCERAMSOC.2019.05.009.

[40] F.J. Martínez-Vázquez, E. Sánchez-González, O. Borrero-López, P. Miranda, A. Pajares, F. Guiberteau, Novel bioinspired composites fabricated by robocasting for dental applications, Ceram. Int. 47 (15) (Aug. 2021) 21343–21349, https://doi.org/10.1016/J.CERAMINT.2021.04.142.

[41] A. Hadian, et al., Material extrusion based additive manufacturing of large zirconia structures using filaments with ethylene vinyl acetate based binder composition, Addit. Manuf. 47 (Nov. 2021), https://doi.org/10.1016/J.ADDMA.2021.102227.

[42] L.M. Rueschhoff, J.P. Youngblood, R.W. Trice, R. Bordia, Stabilizing highly loaded silicon nitride aqueous suspensions using comb polymer concrete superplasticizers, J. Am. Ceram. Soc. 99 (12) (Dec. 2016) 3857–3865, https://doi.org/10.1111/JACE.14432.

[43] E.M. Seftel, S. Mullens, V. Meynen, P. Cool, B. Michielsen, Development of monodisperse porous microspheres of MgAl-layered double hydroxide by droplet coagulation, Powder Technol. 391 (Oct. 2021) 334–343, https://doi.org/10.1016/J.POWTEC.2021.06.021.

[44] M. Lorenz, A. Martin, K.G. Webber, N. Travitzky, Electromechanical Properties of Robocasted Barium Titanate Ceramics 2000325 (2020) 1–10, https://doi.org/10.1002/adem.202000325.

[45] E. Feilden, E.G.T. Blanca, F. Giuliani, E. Saiz, L. Vandeperre, Robocasting of structural ceramic parts with hydrogel inks, J. Eur. Ceram. Soc. 36 (10) (2016) 2525–2533, https://doi.org/10.1016/j.jeurceramsoc.2016.03.001.

[46] J.R. Gomes, F.J. Oliveira, R.F. Silva, M.I. Osendi, P. Miranzo, Effect of α-/β Si3N4-phase ratio and microstructure on the tribological behaviour up to 700°C, Wear 239 (1) (2000) 59–68, https://doi.org/10.1016/S0043-1648(99)00367-1.

[47] J. Zheng, et al., Roughness surface of raspberry-shaped silica nanoparticles effect on shear thickening colloidal suspensions, Appl. Surf. Sci. 606 (2022), 154917, https://doi.org/10.1016/j.apsusc.2022.154917.

[48] M. Blair, C. Ness, Shear thickening in dense suspensions driven by particle interlocking, J. Fluid Mech. 948 (2022), https://doi.org/10.1017/jfm.2022.720.A48.

[49] Y. Yang, D. Cai, Z. Yang, X. Duan, P. He, Rheology of organics-free aqueous ceramic suspensions for additive manufacturing of dense silicon nitride ceramics, Ceram. Int. 48 (21) (2022) 31941–31951, https://doi.org/10.1016/j.ceramint.2022.07.130.

[50] S. Eqtesadi, A. Motealleh, P. Miranda, A. Lemos, A. Rebelo, J.M.F. Ferreira, A simple recipe for direct writing complex 45S5 Bioglass?? 3D scaffolds, Mater. Lett. 93 (2013) 68–71, https://doi.org/10.1016/j.matlet.2012.11.043.

[51] M. Li, et al., Preparation and properties of Si3N4 ceramics via digital light processing using Si3N4 powder coated with Al2O3-Y2O3 sintering additives, Addit. Manuf. 53 (2022), 102713, https://doi.org/10.1016/j.addma.2022.102713.

[52] F.J. Oliveira, R.F. Silva, J.M. Vieira, The reaction rate at Si3N4/steel interfaces as a function of sintering aids, J. Eur. Ceram. Soc. 22 (14–15) (2002) 2561–2570, https://doi.org/10.1016/S0955-2219(02)00117-6.

[53] R.F. Silva, J.M. Gomes, A.S. Miranda, J.M. Vieira, Resistance of Si3N4 ceramic tools to thermal and mechanical loading in cutting of iron alloys, Wear 148 (1) (1991) 69–89, https://doi.org/10.1016/0043-1648(91)90207-B.

[54] V.A. Izhevskiy, L.A. Genova, J.C. Bressiani, F. Aldinger, Progress in SiAlON ceramics, J. Eur. Ceram. Soc. 20 (13) (2000) 2275–2295, https://doi.org/10.1016/S0955-2219(00)00039-X.

[55] T.S. Yen, W.Y. Sun, Phase relationship studies of silicon nitride system—a key to materials design, MRS Online Proc. Libr. 287 (1) (1992) 39–50, https://doi.org/10.1557/proc-287-39.
[56] J. Luo, R. Stevens, Porosity-dependence of elastic moduli and hardness of 3Y-TZP ceramics, Ceram. Int. 25 (1998) 281–286.
[57] D. Gl, B. Tk, R. Mj, Properties and selection: nonferrous alloys and special-purpose materials, in: ASM International Handbook vol. 2, American Society for Metals, Materials Park, 1990, pp. 583–588.
[58] I. Ferreira, P. Cipriano, L. Pessanha, K. Strecker, M. Fellipe, R. Pais, Experimental analysis and numerical simulations of the mechanical properties of a (Ce ,Y) -TZP/Al2O3/H6A ceramic composite containing coupled toughening mechanisms, J. Mech. Behav. Biomed. Mater. 129 (2022), 105171, https://doi.org/10.1016/j.jmbbm.2022.105171.
[59] G.A. Levesque, N.K. Arakere, Critical flaw size in silicon nitride ball bearings, Tribol. Trans. 53 (4) (2010) 511–519, https://doi.org/10.1080/10402000903491291.
[60] Y.-W. Kim, M. Mitomo, N. Hirosaki, R-curve behaviour and microstructure of sintered silicon nitride, J. Mater. Sci. 30 (1995) 5178–5184.
[61] C.-W. Li, S. C Lui, J. Goldacker, Relation between strength, microstructure, and grain-bridging characteristics in in situ reinforced silicon nitride, J. Am. Ceram. Soc. 78 (2) (1995) 449–459, https://doi.org/10.1111/J.1151-2916.1995.TB08823.X.
[62] S. Liu, F. Ye, L. Liu, Q. Liu, Feasibility of preparing of silicon nitride ceramics components by aqueous tape casting in combination with laminated object manufacturing, Mater. Des. 66 (2015) 331–335, https://doi.org/10.1016/j.matdes.2014.10.079. Elsevier Ltd.
[63] J. Zhang, F. Ye, D. Jiang, M. Iwasa, Preparation of bulk Si3N4 from tape casting and lamination, Ceram. Int. 32 (3) (2006) 277–282, https://doi.org/10.1016/j.ceramint.2005.03.003.
[64] B. Cappi, E. Özkol, J. Ebert, R. Telle, Direct inkjet printing of Si3N4: characterization of ink, green bodies and microstructure, J. Eur. Ceram. Soc. 28 (13) (2008) 2625–2628, https://doi.org/10.1016/j.jeurceramsoc.2008.03.004.
[65] Y. Liu, et al., Stereolithographical fabrication of dense Si3N4 ceramics by slurry optimization and pressure sintering, Ceram. Int. 46 (2) (2020) 2063–2071, https://doi.org/10.1016/j.ceramint.2019.09.186.
[66] S. Yu, et al., Fabrication of Si3N4–SiC/SiO2 composites using 3D printing and infiltration processing, Ceram. Int. 47 (20) (2021) 28218–28225, https://doi.org/10.1016/j.ceramint.2021.06.235.